RESEARCH ARTICLE

A Systematic Approach to Digital Control Development for Four-Phase SRM Drive Using Single Current Sensor for Medium Power Applications

T. FAHEEM ALI, (Graduate Student Member, IEEE), **D. ARUN DOMINIC**, (Member, IEEE), **AND PRAJOF PRABHAKARAN**, (Senior Member, IEEE)

Department of Electrical and Electronics Engineering, National Institute of Technology Karnataka, Surathkal, Mangalore, Karnataka 575025, India

Corresponding author: T. Faheem Ali (faheemali.197ee010@nitk.edu.in)

ABSTRACT In the realm of medium-power high-volume applications, Switched Reluctance Motor (SRM) drives hold great advantages over other motors. However, the SRM drive must be optimized to reduce cost without compromising the performance for medium power applications. This paper presents a novel SRM drive utilizing a Miller converter-fed SRM motor with a single current sensor, offering a comprehensive control development procedure encompassing system modeling, design procedures, dynamic simulation, analysis, and experimental validation. The SRM is characterized through finite element analysis (FEA) to derive a MATLAB Simulink simulation model, and the conduction angle is optimized for drive efficiency through parametric simulation studies. The linear SRM model for control design is obtained via small signal analysis. Speed and current controllers are designed using the K-factor method, and the efficacy of the proposed drive is rigorously evaluated across various operating modes in MATLAB Simulink. Additionally, a hardware prototype is developed and the digital control algorithm is implemented on the DSP microcontroller TMS320F28379D based on the designed controllers to further assess drive performance. The results obtained validate the robustness and dynamic performance of the SRM drive across variable speed, variable torque, and constant power modes of operation.

INDEX TERMS Switched reluctance motor (SRM), linearized model, control design, speed control, current control, medium power applications.

I. INTRODUCTION

The preferred motor choices for various applications include permanent magnet motors and Induction Motors (IM) due to their reliability and established technology. Permanent magnet motors, especially those utilizing high-energy rare-earth magnets like Neodymium Iron Boron and Samarium Cobalt, offer higher power density and are more efficient [1], [2], [3]. However, extracting and processing rare earth minerals incurs higher costs and raises environmental concerns [4], [5]. To address these concerns, researchers and manufacturers have been exploring alternatives such as ferrite magnets, which are more abundant but exhibit lower magnetic strength than rare-earth magnets [5]. Additionally, operating at high speeds with weakened magnetic fields in permanent magnet motors reduces the motor's overall efficiency [4], [5]. Conversely, the Switched Reluctance Motor (SRM) offers a simple design characterized by a doubly salient structure, avoiding the need for permanent magnets and rotor conductors. Additionally, SRM's merits encompass efficient operation at elevated temperatures, superior fault tolerance, and reduced rotor losses attributed to the absence of rotor windings [6]. As a result, SRM stands as a more robust and efficient option compared to IM, potentially translating to heightened affordability and efficacy across various applications [6], [7], [8].

The associate editor coordinating the review of this manuscript and approving it for publication was Xueguang Zhang.

In the context of medium power applications, optimizing both converter and control strategies is crucial within cost constraints, aiming to minimize costs without compromising drive performance. The asymmetric H-bridge (AHB) converter, a popular choice for SRM, with $2n$ switches and diodes for an n-phase SRM, offers advantages such as independent phase current control and faster demagnetization. Numerous literature sources, such as [4], [9], and [10] explore various converter configurations for SRM drives. Reference [11] proposes an asymmetric three-level neutral point diode clamped converter for SRM drives which are typically useful for high power applications, since it has more number of switches than conventional AHB converter. Among these, the Miller converter [12] stands out for its utilization of $2(n - 2)$ switches for an n-phase SRM. This topology maintains both phase independence and demagnetization efficiency, making it a notable choice for reduced switch SRM applications.

In addition to cost-effective converters, control methods with lower computational intensity and reduced memory requirements are crucial for medium-power applications. Minimizing the number of sensors is also imperative. While absolute position encoders are commonly used for precise rotor positioning in SRM control, position sensorless control strategies [13] offer alternatives. The SRM position-sensorless control typically relies on acquiring flux linkage or inductance, which vary with rotor position, to estimate the rotor position. In [14], an incremental-inductance estimation method for position sensing is analyzed. The implementation is simple but provides inaccurate position estimation at lower speeds. For accurate speed estimation across a wide range of speeds, a method employing high-frequency voltage injection during the idle phase is employed in [15]. However, this involves additional voltage injection power losses. These require a position lookup table based on flux linkage-position-phase current characteristics of the SRM. In [16], the 3D lookup table is obtained by numerical methods and a third-order phase-locked loop (PLL) is designed to reduce estimation error. These position sensorless schemes in [14], [15], and [16] require a 3D lookup table to be stored in the controller to estimate the position, taking up a significant amount of memory space. Additionally, position sensorless SRM control requires phase current measurement to estimate the phase inductance. In [17], a cost-effective current measurement technique for 4-phase SRM by split dual bus line without pulse injection and voltage penalty is proposed. An online sensorless position estimation for SRM using one current sensor is proposed in [18]. However, these methods demand higher memory space or computational capabilities, leading to a preference for dedicated position encoders in medium-power applications.

Considering current sensors, a conventional SRM drive typically employs n number of current sensors for an n-phase SRM motor. To overcome this issue, [19] suggests a v/f strategy, controlling the input voltage instead of phase currents and hence reducing the sensor count. However, this results in increased torque ripple. In [20], the authors have proposed an innovative SRM drive with single and dual current sensors for the conventional AHB converter, addressing torque ripple. However, this work lacks detailed control development, and a systematic control design is missing.

In addition to prioritizing cost-effective converters and minimizing the number of sensors, control methods with lower computational intensity and reduced memory requirements are crucial for medium-power applications. Various control strategies for SRM drives have been proposed and developed in the literature, focusing on digital implementation with low-cost microcontrollers. For instance, in [21], the authors designed and laboratory-tested a 5-hp SRM drive using an Intel 8751 microcomputer, known for its affordability as a digital controller. This work specifically featured the design and implementation of a speed or torque controller using current delta modulation. Similarly, the authors of [22] adopted the same control strategy for an SRM drive, employing delta modulation but implementing it on the TMS320C30 Digital Signal Processor (DSP). While the delta modulation PWM technique offers a fixed-frequency modulation method that is easy to implement in digital controllers, it comes with the drawback of increased current ripple due to fixed sampling intervals, potentially impacting motor performance and efficiency [23]. Also, in [21] and [22], the non-linear dynamic characteristics of SRM are not analyzed in detail to decide the conduction angle. Reference [24] uses a non-linear analytical flux function to figure out the conduction angle. In this work, the authors have designed a non-linear state feedback controller to handle the non-linearities described by this function. However, often, the analytical flux function does not accurately align with actual motor dynamics.

In [25], an innovative control strategy called direct instantaneous torque control (DITC) employing a torque hysteresis controller is proposed. However, this requires a pre-estimated rotor torque look-up table to calculate the instantaneous torque. A sliding mode DITC cruise control for SRM, where the turn-off angle is controlled using a minimum torque ripple point tracker, is proposed in [26]. However, both [25] and [26] require prior torque characteristics stored in the microcontroller or computationally intensive online optimization techniques. This complexity makes them unsuitable for medium-power SRM drive applications. Current hysteresis control is another popular method implemented for SRM drives, where motor phase currents are controlled and regulated within a hysteresis band. Although effective in maintaining current within a desired band, its variable switching frequency poses challenges for digital implementation. The use of PI controllers mitigates the above-mentioned issue, operates the SRM drive with a fixed switching frequency, and ensures lower current ripple [27]. Additionally, using a linear controller makes it easier to
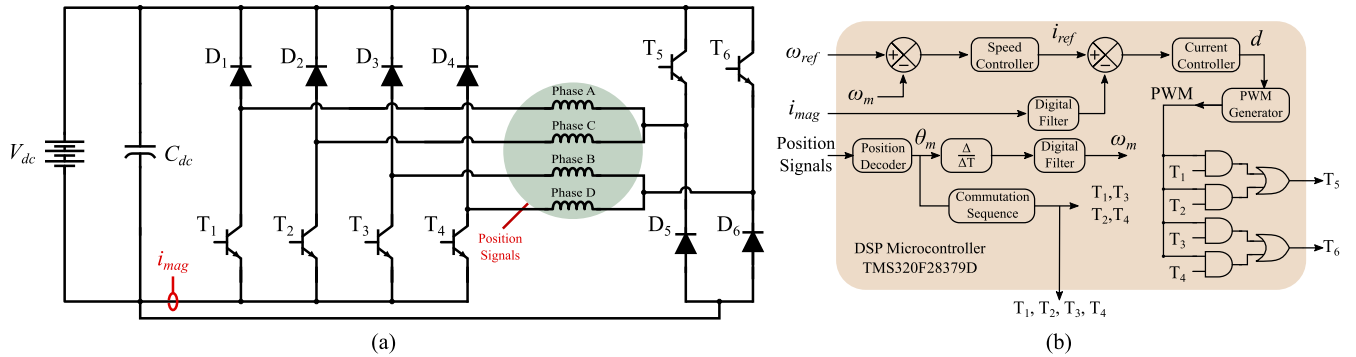
FIGURE 1. The proposed SRM drive. (a) The circuit configuration of the Miller converter fed the SRM drive utilizing a single current sensor. (b) The block diagram depicting the control logic.

utilize the PWM module in DSPs and synchronize with other control systems. Different fixed frequency control strategies for SRM drives are reviewed in [28]. However, to the best of the authors' knowledge, there are no research papers in the literature that present a systematic approach to digital control development for an SRM drive using a single current sensor for medium-power applications.

In summary, the literature offers various control strategies, but for medium-power applications, SRM drives with a dedicated position sensor and a fixed control strategy based on a linearized transfer function are particularly relevant. Despite this, a comprehensive control development procedure is lacking in the existing literature. This paper addresses this gap by presenting a novel SRM drive with a Miller converter-fed SRM motor, utilizing a single current sensor for medium-power applications. The paper outlines a systematic development of controllers, covering system modeling, design procedures, dynamic simulation, analysis, and experimental validation.

The characterization of the SRM is carried out using finite element analysis (FEA) to derive the MATLAB Simulink simulation model. Additionally, based on parametric simulation studies, the conduction angle is selected to maximize drive efficiency. The linear model of the SRM for control design is obtained through small signal analysis [9], [29]. Subsequently, speed and current controllers are designed using the K-factor method outlined in [30]. The proposed drive's efficacy is thoroughly evaluated across various operating modes using MATLAB Simulink. To further assess drive performance, a hardware prototype is developed in the laboratory, and the digital control algorithm is developed and implemented on the DSP microcontroller TMS320F28379D based on the designed controllers.

The rest of this paper is structured as follows: In the second section, the operation of the proposed drive is introduced. In the third section, the development of a simulation model using FEA is detailed. The fourth section delves into the derivation of the SRM motor's small signal model and system transfer function, followed by the fifth section detailing the controller design. The sixth section presents simulation

results and a detailed analysis. Subsequently, the seventh section highlights the control algorithm, presents hardware results, and offers an in-depth analysis. Finally, the eighth section concludes the paper, summarizing findings and insights.

II. PROPOSED SYSTEM

The proposed converter topology and control scheme are illustrated in Fig. 1. As shown in Fig. 1(a), the system utilizes a Miller converter, which, in the case of a four-phase SRM, results in a reduction in the number of switches and diodes compared to an AHB converter. Specifically, the Miller converter employs six switches and six diodes, while the AHB converter necessitates eight switches and eight diodes. By sharing one leg between two non-adjacent phase windings in the power converter, independent current control in all phases is achieved. Consequently, this design effectively mitigates extended demagnetization times. Despite the uneven distribution of heating losses among devices, it notably enhances control flexibility.

The proposed system incorporates a single current sensor strategically placed to measure phase currents during magnetization. To achieve this, the magnetizing and demagnetizing paths are decoupled, as depicted in Fig. 1, which also shows the operational modes for phase A of the proposed SRM drive. In the control scheme, only one phase is excited at a time, allowing the current sensor to measure the individual phase current when the corresponding phase is active. Consequently, independent control of this drive is feasible with just a single current sensor.

As shown in Fig. 1(b), the control scheme employs a dual loop with inner current control and an outer speed control loop. The controller's inputs include the speed reference, the sensed current through the magnetizing path (i_{mag}), and position signals. A position sensor is utilized to gather position information, and both speed (ω_m) and position (θ_m) are derived from these signals. The measured speed (ω_m) goes through a digital low pass filter for noise rejection and is compared with the reference speed (ω_{ref}) and fed into the speed controller, which gives the current reference (i_{ref}).
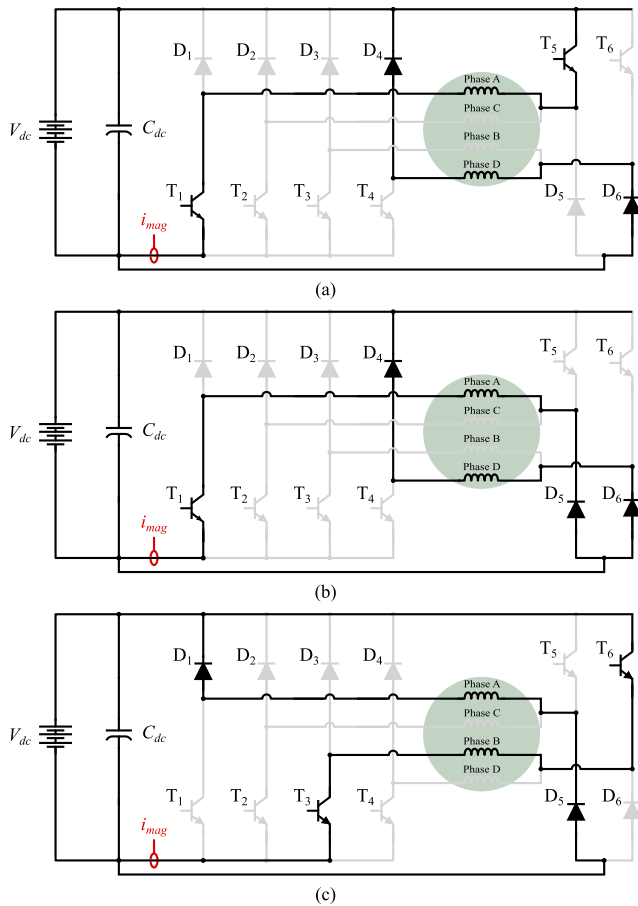
FIGURE 2. Three operating states of phase A during the motoring mode. (a) Magnetization mode. (b) Zero voltage mode. (c) Demagnetization mode.

The measured current through the magnetizing path (i_{mag}) is passed through a low-pass digital filter to filter out the noise, which is then compared with the current reference (i_{ref}). In the proposed switching scheme, switches T_1, T_2, T_3, and T_4 are switched at the fundamental frequency following the commutation sequence. The duty cycle output of the current controller is fed to the PWM generator module and supplied to switches T_5 and T_6 according to the phase sequence.

Fig. 2 is drawn assuming the phase excitation sequence is in a clockwise direction, i.e., D-A-B-C. This sequence is selected to illustrate the operation of the drive during clockwise rotation. As shown in Fig. 2(a), during the commutation of winding D, phase A is excited. To enter the demagnetization region for the D phase, switches T_4 and T_6 are turned off. During this mode, diodes D_4 and D_6 conduct, applying $-V_{dc}$ across phase D, thereby feeding the phase current back to the source until phase D is completely demagnetized. Simultaneously, switches T_1 and T_5 are turned on, applying $+V_{dc}$ across phase A. As in Fig. 2(b), as T_5 is turned off, the phase A current freewheels through switch T_1 and diode D_5. During this period, the voltage across phase A is zero, and the phase current decays due to winding resistive loss. Hence, the phase current is controlled by switching T_5 in

PWM mode at high frequency. In these two modes, only the current through the phase A winding appears in the current sensor output since the magnetization and demagnetization paths are decoupled. Moving to Fig. 2(c), phase A, akin to phase D in Fig. 2(a), undergoes demagnetization as phase B is excited. During this mode, the current sensor measures the current through the phase B winding.

Therefore, it can be inferred that the proposed system, incorporating the Miller converter and employing a single current sensor, presents a cost-effective solution particularly crucial for medium power applications. The control strategy proposed without overlap in the conduction period for different phases ensures optimal drive performance. The control and validation of the proposed are detailed in subsequent sections.

III. MODELING OF SRM FOR SIMULATION

SRMs inherently exhibit nonlinear characteristics, such as magnetic saturation and switching dynamics. For accurate simulations, it is essential to utilize an SRM model that encompasses its inherent nonlinearities. The block diagram depicting the SRM simulation model is shown in Fig. 3. The voltage equation for an SRM can be written as:

$$v_{ph} = i_{ph}R_s + \frac{d\psi_{ph}}{dt}. \tag{1}$$

where v_{ph}, i_{ph}, R_s and ψ_{ph}, are the phase voltage, phase current, stator winding resistance, and flux linkage with the rotor, respectively. From (1), the flux per phase can be derived and is given by:

$$\psi_{ph} = \int_0^t (v_{ph} - i_{ph}R_s)\, dt. \tag{2}$$

Fig. 3(a) shows the block diagram for the corresponding per-phase electrical model of the SRM. In this model, the flux linkage is calculated as per (2). Subsequently, the model incorporates a current look-up table (LUT), offering current values based on the respective flux linkage and rotor position. This is followed by an LUT that provides torque values corresponding to the given current and rotor position. In order to enhance the comprehensiveness and accuracy of the model depicted in Fig. 3(a) and to develop a holistic simulation model, it is imperative to conduct a prior characterization of the SRM. The details of this characterization are provided in the subsequent section of this paper.

The mechanical equation for the torque of the motor is given by

$$T_e(\theta, i) = T_l + J\frac{d\omega_m}{dt} + B\omega_m. \tag{3}$$

where T_e, T_l, ω_m, J, and B represent the generated torque, load torque, mechanical speed, the moment of inertia, and frictional coefficient of the motor, respectively. Fig. 3(b) illustrates the corresponding mechanical model. The net torque is the sum of the individual phase torques.
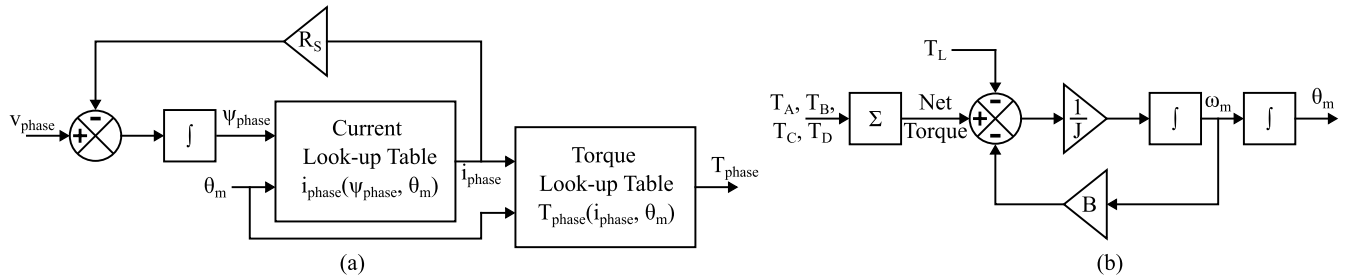
FIGURE 3. Detailed simulation model of the SRM. (a) Per phase SRM electrical model. (b) Mechanical model.

TABLE 1. Machine Parameters.

| Electrical Parameters		Geometrical Parameters	
Parameter	**Value**	**Parameter**	**Value**
Phases	4	Stator poles/rotor poles	8/6
Power	1 hp	Number of Turns	70 turns
Speed	2000 RPM	Length of Core	100 mm
Voltage, Current	380 V, 2.6 A	Stator Outer Diameter	100 mm
Stator Resistance (R_s)	1 Ω	Stator Inner Diameter	60 mm
Moment of Inertia (J)	0.00082 $kg.m^2$	Length of Air Gap	0.5 mm
Coefficient of Friction (B)	0.001 $N.m.s$	Rotor Inner Diameter	19 mm
Unaligned Phase Inductance (L_u)	3.95 mH	Stator pole arc angle (β_s)	19.8°
Aligned Phase Inductance (L_a)	24.6 mH	Rotor pole arc angle (β_r)	24°
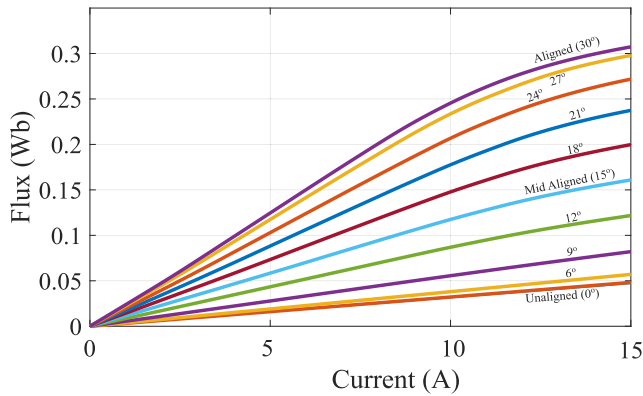
FIGURE 4. The downsampled flux characteristics obtained from SRM characterization using Ansys as in (4).

A. CHARACTERIZATION OF SRM

Several methods exist for characterizing SRMs, ranging from analytical approaches to powerful electromagnetic Finite Element Analysis (FEA) tools. The analytical method, based on known parameters such as aligned inductance, unaligned inductance, maximum current, and maximum flux linkage, is extensively detailed in [31] and [32]. While analytical methods based on known parameters offer simplicity, they often struggle with the intricate nonlinearities inherent in SRMs [4]. For that reason, this work leverages Ansys Maxwell, a robust FEA tool, to achieve a more accurate and comprehensive characterization.

The characterization begins with SRM design in Ansys RMxprt, utilizing the geometrical parameters specified in Table 1. Subsequently, FEA analysis generates flux data
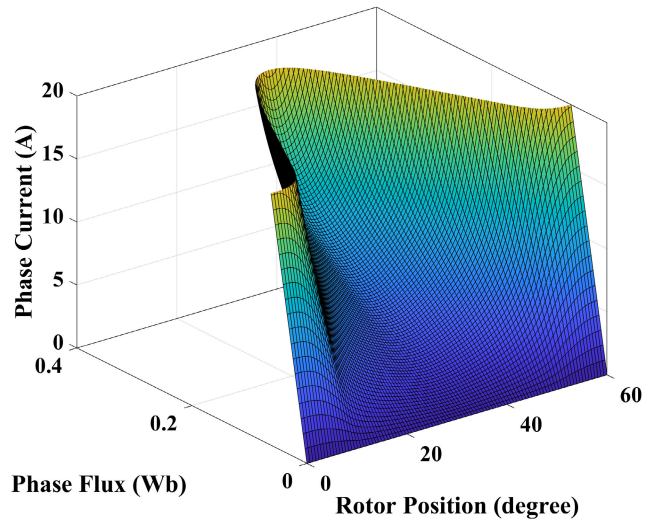

FIGURE 5. Three-dimensional LUT showing phase current versus flux and rotor angle obtained by inverse interpolation of the flux characteristics as in (5).

dependent on both current (i_{ph}) and rotor position (θ_m). However, the raw data might not be uniformly sampled across the current range, requiring interpolation to ensure uniform data distribution for both current and rotor positions. This interpolation then yields a non-linear function representing the flux (ψ_{ph}) as a function of both current and rotor position:

$$\text{Phase Flux} = \psi_{ph}(i_{ph}, \theta_m). \tag{4}$$

To enhance clarity and visual understanding, the dense interpolated flux data is down-sampled, and the resulting plot is presented in Fig. 4.
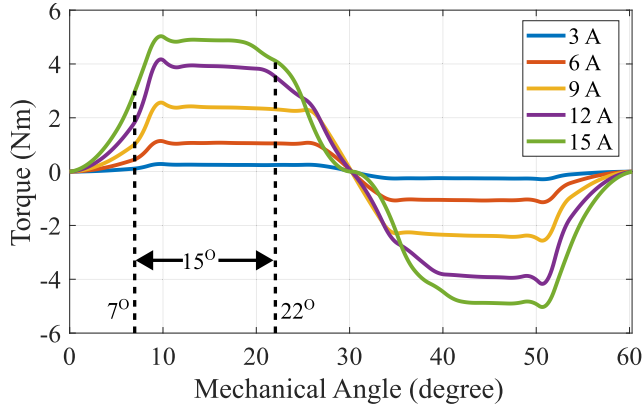
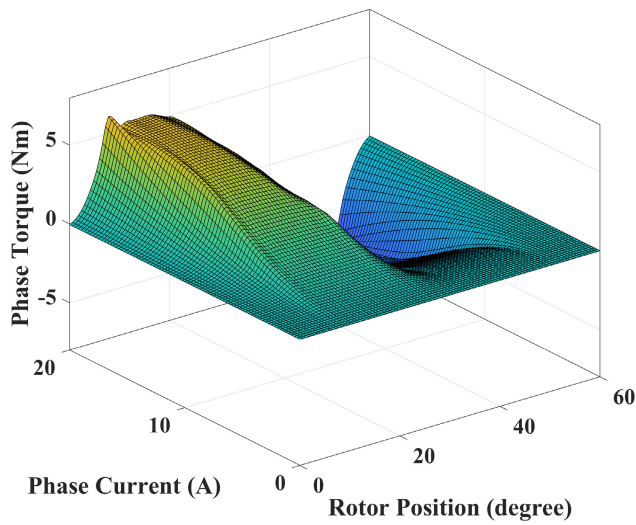**FIGURE 6.** The downsampled torque characteristics obtained as in (7).

FIGURE 7. Three-dimensional LUT showing electromagnetic torque generated versus phase current and rotor angle obtained as in (7).

With the non-linear flux-current-angle relationship established in (4), the phase current Look-Up Table (LUT) for the SRM model is derived. This LUT maps the required current for a given flux and rotor position. This LUT is obtained by performing inverse interpolation on the flux data in (4) for flux values ranging from zero to maximum flux. This determines the corresponding current required to achieve a flux for any given rotor position. Mathematically, this relationship is captured by Equation (5):

$$\text{Phase Current} = i_{ph}(\psi_{ph}, \theta_m). \tag{5}$$

The surface plot illustrating the current LUT obtained is depicted in Fig. 5.

In SRM, for a given current, the incremental mechanical energy required for the rotor to traverse an angle corresponds to the area enclosed between the flux curves at the initial and final rotor positions. Dividing this energy by the angle of rotation provides the mechanical torque. Consequently, the flux data (in (4)) is integrated along the current vector to get

the energy (W) function as:

$$W = \int_0^{i_{ph}} \psi_{ph}(i_{ph}, \theta_m) di_{ph}. \tag{6}$$

The resulting incremental area, divided by the incremental angle, gives the torque:

$$\text{Phase Torque} = \frac{\partial W(i_{ph}, \theta_m)}{\partial \theta_m}. \tag{7}$$

The obtained downsampled torque data is presented in Fig. 6, while the surface plot of the same can be seen in Fig. 7. The LUT for one phase can be used to model all phases by applying a rotor position offset of 15°. The offset of 15° in rotor position is applied to align with the symmetric characteristic of a 4-phase SRM with 6 rotor poles, ensuring accurate representation in the simulation.

Furthermore, the conduction and commutation angles have been fine-tuned to enhance efficiency at the rated power level. As previously explained, given the constraint of using a single current sensor to control phase currents independently, it is imperative to avoid conduction overlap between the phases. Therefore, to ensure only one phase is excited at a time, the conduction angle for each phase is fixed at 15°. Through parameterized simulations and analysis, it has been determined that the maximum efficiency is achieved with a turn-on angle of 7°, while the turn-off angle is set at 22° (7° + 15°). The obtained turn-on and commutation angles are marked in the torque characteristics shown in Fig. 6. Subsequent investigations are conducted with these fixed turn-on and commutation angles.

IV. DERIVATION OF SYSTEM LINEAR MODEL

Linear controllers are typically developed under the assumption of linear system dynamics. As a result, it becomes necessary to derive a linearized model. To facilitate controller design for SRMs, an overall system transfer function must be derived, encompassing not only the linearized motor model but also feedback gains, filters, and other control loop components. In this section, the transfer function is derived while adhering to linear assumptions. This approach is essential for the effective design of control systems, allowing us to address and manage the inherent nonlinearities of the motor.

A. SMALL SIGNAL MODEL OF SRM MOTOR

The small signal model of the SRM is derived from the fundamental voltage and torque equations assuming linear dynamics. The voltage equation in (1) can be written as

$$v_{ph} = i_{ph}R_s + L_{ph}(\theta)\frac{di_{ph}(t)}{dt} + \omega_m\, i_{ph}(t)\frac{dL_{ph}(\theta)}{d\theta}. \tag{8}$$

where the L_{ph} is the inductance per phase, θ is the rotor angle, i_{ph} is the per phase current, and ω_m represents the speed of the rotor. With the same assumption, the torque per phase can be written as

$$T_{ph} = \frac{1}{2}i_{ph}^2(t)\frac{dL_{ph}(\theta)}{d\theta}. \tag{9}$$
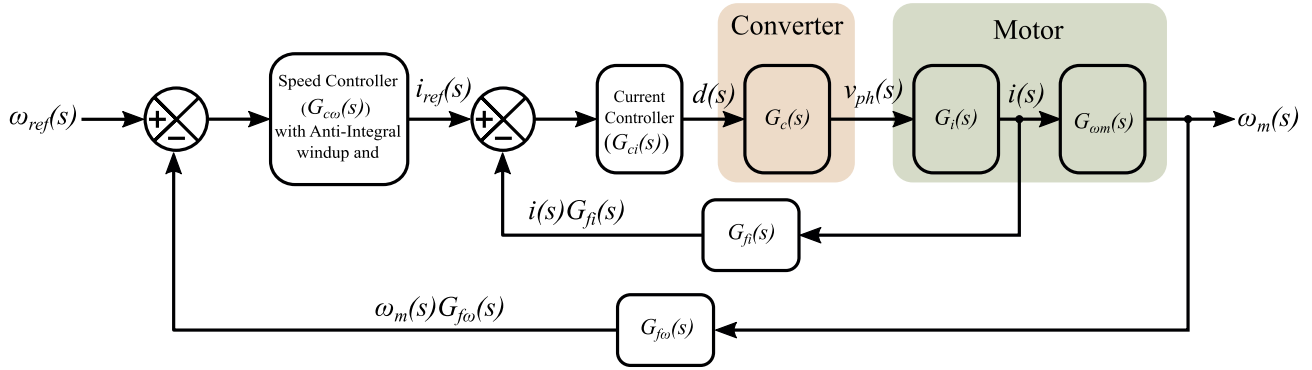
FIGURE 8. Block diagram for the speed control of the proposed SRM drive.

Assuming there is no overlap in phase currents. i.e., only one phase conducts at a time, the per phase voltage equation and electromagnetic torque equation in (3), (8), and (9) can be written as below:

$$v_{ph} = iR_s + L(\theta)\frac{di(t)}{dt} + \omega\, i(t)\frac{dL(\theta)}{d\theta} \quad (10)$$

$$J\frac{d\omega_m}{dt} = \frac{1}{2}i^2(t)\frac{dL(\theta)}{d\theta} - T_l - B\omega_m \quad (11)$$

where, i represents the sum of the phase currents, assuming no overlap in phase currents. Also, L_{ph} is represented as L to simplify the equation. By perturbing and linearizing the system around a steady-state operating point characterized by a speed of ω_{m0} and current of i_0, the state space model of SRM can be obtained. The state-space representation of the SRM is given by:

$$\dot{x} = Ax + B'u$$
$$Y = Cx + Du.$$
$$where, x = \begin{bmatrix} i \\ \omega_m \end{bmatrix} and\ u = \begin{bmatrix} v \\ T_l \end{bmatrix}. \quad (12)$$

The state-space model is further elaborated as follows:

$$\dot{x} = \begin{bmatrix} -\dfrac{R_s}{L} - \dfrac{1}{L}\dfrac{dL}{d\theta}\omega_{m0} & -\dfrac{1}{L}\dfrac{dL}{d\theta}i_0 \\[2ex] \dfrac{1}{J}\dfrac{dL}{d\theta}i_0 & -\dfrac{B}{J} \end{bmatrix} x + \begin{bmatrix} \dfrac{1}{L} & 0 \\[2ex] 0 & -\dfrac{1}{J} \end{bmatrix} u. \quad (13)$$

The inductance slope in the torque-generating region is assumed to be constant, and the average inductance is assumed to be the average of aligned and unaligned inductances. Thus,

$$\frac{dL}{d\theta} = \frac{L_a - L_u}{\beta_s} \ ; \ L = \frac{L_a + L_u}{2}. \quad (14)$$

where L_a, L_u, and β_s are aligned inductance, unaligned inductance, and stator pole arc angle of the SRM motor. To simplify the design of the linear controller, we can extract relevant transfer functions from the state space model as

following:

$$G_i(s) = \frac{i(s)}{v_{ph}(s)};\ for\ C = \begin{bmatrix} 1 & 0 \end{bmatrix} \quad (15)$$

$$G(s) = \frac{\omega_m(s)}{v_{ph}(s)};\ for\ C = \begin{bmatrix} 0 & 1 \end{bmatrix} \quad (16)$$

From (15) and (16), G_{ω_m} can be obtained as below:

$$G_{\omega_m}(s) = \frac{G(s)}{G_i(s)} \quad (17)$$

With the SRM small signal model, the converter and feedback filters need to be modeled for control design.

B. SYSTEM TRANSFER FUNCTION
The block diagram for the per-phase control can be seen in Fig. 8. The expression for the average output voltage of the soft-chopped converter, denoted as V_{ph}, during a switching cycle T_s is given by:

$$V_{ph} = V_{dc}d + 0 \cdot (1 - d) = d \cdot V_{dc}. \quad (18)$$

In the soft-chopped converter, the output voltage switches between $+V_{dc}$ and zero or $-V_{dc}$ and zero. Due to the nature of pulse width modulation, there is a delay of half the switching period T_s, which can be represented as a pole with a time constant $\tau_d = T_s/2$. For a switching frequency of 10 kHz, T_d is equal to 50 μs. Thus, the converter transfer function is given by:

$$G_c(s) = \frac{v_{ph}(s)}{d(s)} = \frac{V_{dc}}{1 + s\tau_d}. \quad (19)$$

The current feedback transfer function is of a low-pass type, designed to eliminate high-frequency components. It corresponds to a first-order filter with a time constant τ_{fi}, resulting in a pole at 8 kHz (10 times the current controller corner frequency). Therefore:

$$G_{fi}(s) = \frac{1}{1 + s\tau_{fi}};\ \tau_{fi} = \frac{1}{2\pi\,8000}. \quad (20)$$

Similarly, the speed feedback transfer function is also a first-order low-pass filter with a time constant $\tau_{f\omega_m}$ corresponding
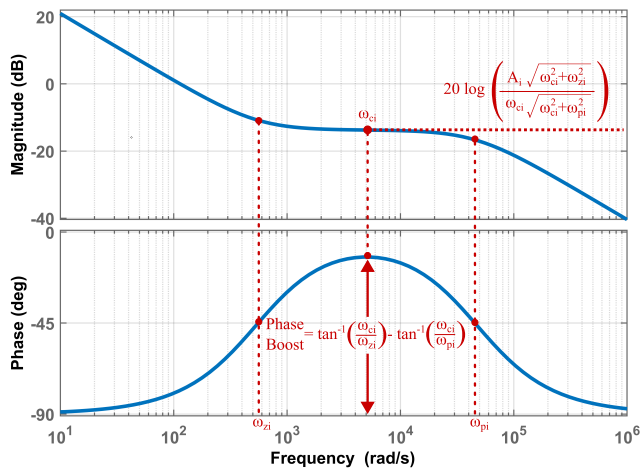
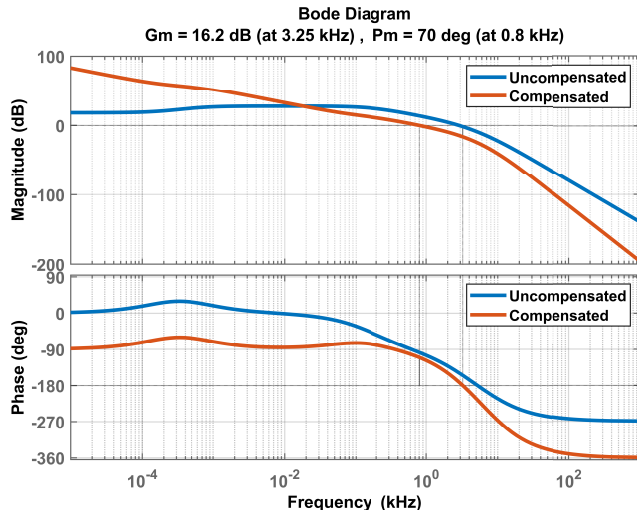**FIGURE 9.** Bode plot of the current controller, G_{ci} (Type II Compensator).

FIGURE 10. Bode plots of plant transfer function (G_{pi}) and loop transfer function ($G_{pi} \cdot G_{ci}$) for closed-loop current control.
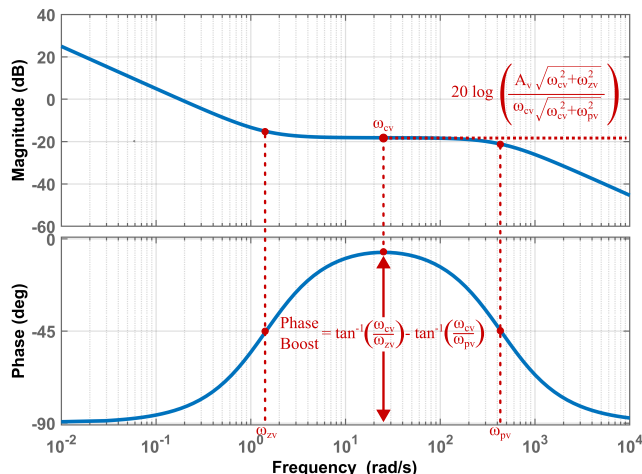
to a pole at 1000 Hz:

$$G_{f\omega_m}(s) = \frac{1}{1 + s\tau_{f\omega_m}}; \quad \tau_{f\omega_m} = \frac{1}{2\pi\ 1000}. \tag{21}$$

Now, we can derive the plant transfer functions for the current controller design and speed controller design. The equivalent plant transfer function for the current controller design is:

$$G_{pi}(s) = G_c \cdot G_{fi} \cdot G_i(s). \tag{22}$$

Similarly, the equivalent plant transfer function for the speed controller design is:

$$G_{p\omega_m}(s) = \frac{G_{ci} \cdot G_c \cdot G_i}{1 + G_{ci} \cdot G_c \cdot G_i \cdot G_{fi}} \cdot G_{\omega_m} \cdot G_{f\omega_m}. \tag{23}$$

The electrical parameters of the SRM drive are given in Table 1. The system transfer function is obtained for the known parameters.

V. CONTROLLER DESIGN AND IMPLEMENTATION
A. K FACTOR METHOD
For the obtained plant transfer functions, type II compensators are designed using the K-Factor approach [30]. Initially, the current controller is designed for the current loop plant transfer function given in (22). The controller bandwidth is set to 800 Hz ($\omega_{ci} = 1600\pi$), considering the switching frequency of 10 kHz. To minimize transient ripple in the phase current and consequent torque ripple, a desired phase margin of 70° is chosen. The type II compensator transfer function is given by

$$G_{ci}(s) = \frac{A_i}{s} \frac{s + \omega_{zi}}{s + \omega_{pi}}. \tag{24}$$

In the controller design process, the phase boost required for the loop transfer function ($G_{pi} \cdot G_{ci}$) to achieve the desired phase margin at the controller cutoff frequency (ω_{ci}) is calculated. Subsequently, the controller zero (ω_{zi}) and pole

FIGURE 11. Bode plot of the speed controller, $G_{c\omega_m}$ (Type II Compensator).

(ω_{pi}) are determined, and the controller gain (A_i) is adjusted to achieve unity gain at the controller cut-off frequency. The bode plot for the resulting current controller is shown in Fig. 9, with bode plots for the plant transfer function (G_{pi}) and the loop transfer function ($G_{pi} \cdot G_{ci}$) presented in Fig. 10.

Similarly, the speed controller for the plant transfer function in (23) is designed for a bandwidth of 4 Hz with a desired phase margin of 80°. The type II transfer function is given by

$$G_{c\omega_m}(s) = \frac{A_{\omega_m}}{s} \frac{s + \omega_{z\omega_m}}{s + \omega_{p\omega_m}}. \tag{25}$$

The bode plot for the obtained speed controller is shown in Fig. 11. The bode plots for the plant transfer function ($G_{p\omega_m}$) and loop transfer function ($G_{p\omega_m} \cdot G_{c\omega_m}$) are provided in Fig. 12.
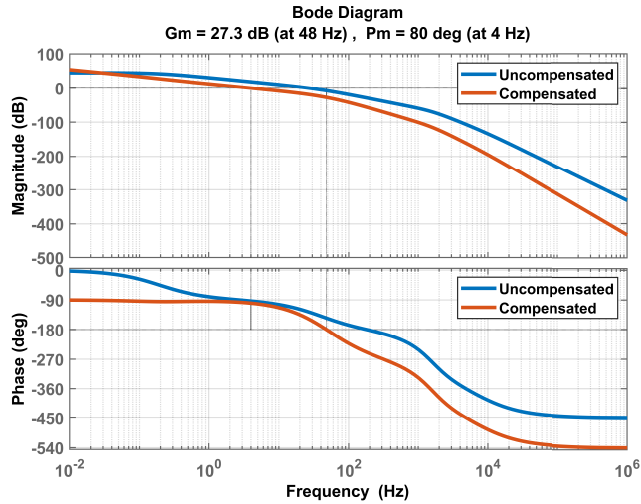
FIGURE 12. Bode plots of plant transfer function ($G_{p\omega_m}$) and loop transfer function ($G_{p\omega_m} \cdot G_{c\omega_m}$) for closed-loop speed control.
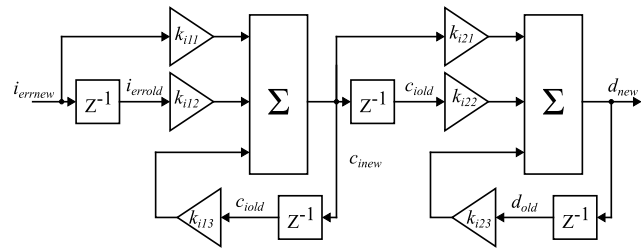

FIGURE 13. Discretized current controller model.

B. DESCRETIZATION OF CONTROLLERS AND INTEGRAL ANTI-WINDUP USING BACK CALCULATION METHOD

The obtained controllers are in the continuous domain. Hence, the discretization of linear controllers is essential for implementing control algorithms in digital control systems. This discrete-time operation requires converting continuous-time controllers and system models into discrete-time equivalents. Additionally, finite precision and hardware limitations in digital systems must be considered, which can introduce quantization errors. Ensuring stability in the discrete-time domain, adjusting controller parameters, and addressing computational constraints are vital aspects of this process. The current controller transfer function shown in (24) is discretized using bilinear transformation for a sampling frequency of 20 μs. The discretized model of the current control transfer function is shown in Fig. 13. Constants, $k_{i11}, k_{i12}, k_{i13}, k_{i21}, k_{i22}$, and k_{i23} corresponds to the gain values in discrete current controller.

The motor operates as a system with higher inertia. To prevent the current from exceeding its rated value, it is essential to introduce saturation to the current reference. Without this saturation, a substantial overshoot in the current reference could occur, posing a risk during startup or transient load changes. Therefore, implementing saturation is crucial to safeguard the motor drive. While saturation is already applied to the controller's output, there remains a possibility of overshooting in the integral component. This can occur due
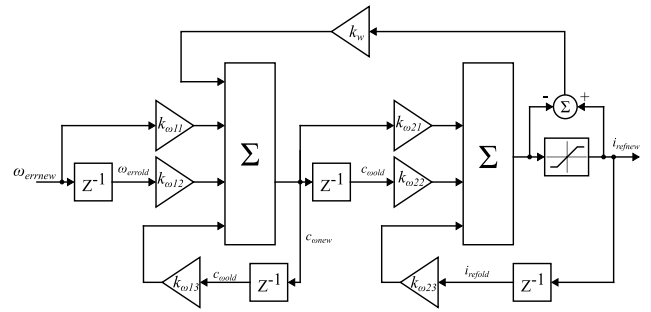

FIGURE 14. Discretized speed controller model with saturation and integral windup.
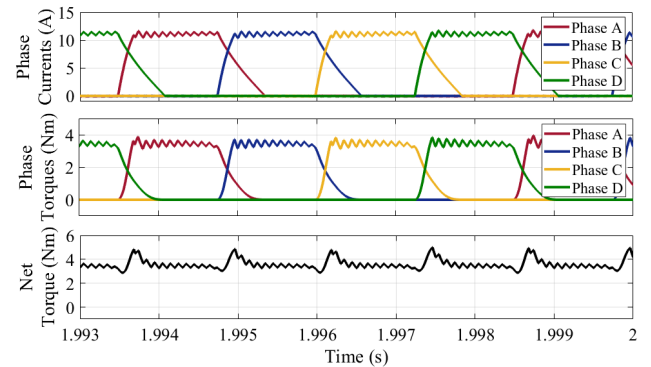

FIGURE 15. Simulation results showing phase currents, phase torques, and net torque at 2000 rpm.

to the integral action continuing to accumulate errors even when the system is saturated. To address this concern, the implementation of integral anti-windup becomes essential. This mechanism helps prevent the integral component from excessively accumulating error during saturation, thereby mitigating the risk of overshoot and instability.

Similar to the current controller, the speed controller transfer function shown in (25) is discretized using bilinear transformation for a sampling frequency of 20 μs. Anti-integral windup are explored for PID-based control systems in [33] and [34]. Here, a back calculation-based anti-windup strategy is developed for the designed discrete controller as shown in 14. The controller gains $k_{\omega 11}, k_{\omega 12}, k_{\omega 13}, k_{\omega 21}, k_{\omega 22}$, and $k_{\omega 23}$ corresponds to the discretized speed controller transfer functions. On the other hand, the parameter k_w is associated with the anti-windup constant, which governs the rate of integral term reset. The control algorithm for hardware implementation is described in the next section.

VI. SIMULATION RESULTS

The model described in III is utilized for the simulation studies. The simulation is carried out to validate and verify the operation of the proposed SRM drive and to validate the control strategy and design detailed in previous sections.

Fig. 15 showcases individual phase currents, phase torques, and the net torque at 2000 rpm. Notably, the designed current controller effectively regulates the phase currents within a satisfactory tolerance band, even without relying on
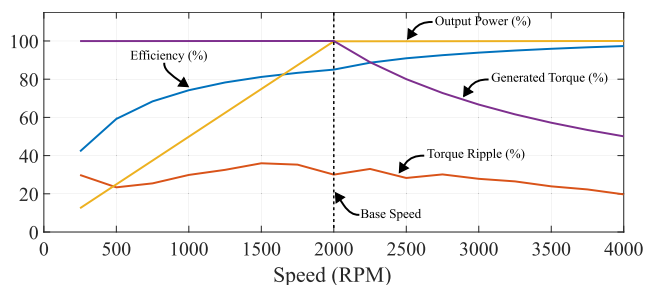
FIGURE 16. Drive characteristics obtained from simulation analysis showing output torque, output power, efficiency, and torque ripple across a wide range of speed.
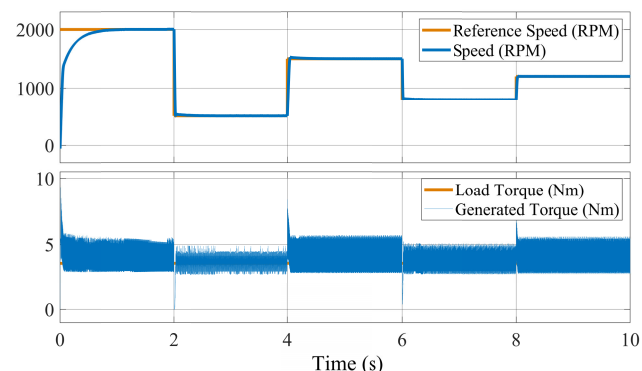

FIGURE 17. Simulation results showing reference speed, speed, load torque and output torque during dynamic step changes in speed reference at constant load torque.

FIGURE 18. Simulation results showing reference speed, speed, load torque and output torque during dynamic step changes in speed reference in constant power region above base speed.

FIGURE 19. Simulation results showing reference speed, speed, load torque and output torque during dynamic step changes in load torque at constant speed reference of 2000 rpm.

hysteresis control. This demonstrates its efficacy and offers a simpler and more reliable alternative to techniques like hysteresis or delta modulation. Furthermore, the plot reveals the torque sharing between phases achieved by the employed control strategy, with the net torque representing the sum of individual phase torques. Evidently, while only one phase operates in magnetization mode, the torque generated by the demagnetization current facilitates torque sharing at the commutation points.

Fig. 16 provides insight into the efficiency and torque ripple across a wide speed range with a fixed conduction period. Notably, the net torque exhibits a maximum torque ripple of 29.8% at 250 rpm with a 12% load and a minimum of 19% at 4000 rpm under full load. Furthermore, the drive displays its lowest efficiency of 42.2% at 250 rpm with a 12% load, while achieving maximum efficiency of 97.34% at 4000 rpm under full load. At the rated speed and power, the drive maintains a torque ripple of 29% and an efficiency of 85%. These results collectively validate the suitability of the SRM for a wide array of applications.

To comprehensively evaluate the control design's effectiveness, an in-depth simulation is carried out, analyzing the drive's performance across various operational scenarios. These scenarios encompass variable speed control, variable torque control, and constant power control at speeds exceeding the base speed. In Fig. 17, the dynamic performance of the drive during variable speed control under constant load torque is illustrated. Operating at a load torque of 3.58 Nm,
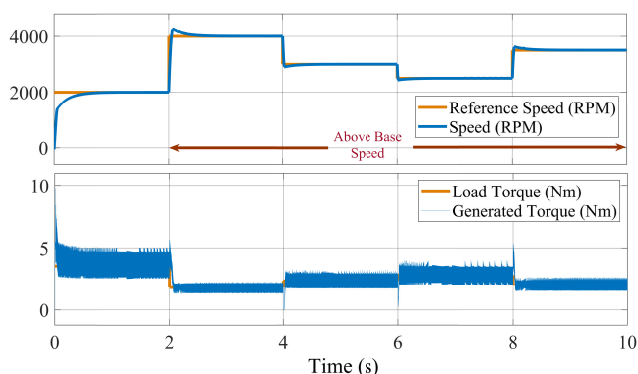
the motor seamlessly tracks the reference speed, exhibiting neither overshoot nor undershoot. Fig. 18 presents the speed and generated torque in the constant power region above the base speed. In this mode, power is set to the rated 750 W, and the results demonstrated accurate tracking of the speed reference. Fig. 19 shows the dynamic performance of the drive in constant speed mode with variable load torque. The speed is regulated at the rated speed of the motor of 2000 rpm. Minor amplitude overshoots or undershoots occurred during step changes in load torque, but the speed promptly stabilized thereafter.

Across all three figures (Fig. 17, Fig. 18, and Fig. 19), it is evident that the integration of anti-windup effectively mitigated speed overshoots and minimized delays in tracking the reference speed, especially during startup and dynamic speed variations. Furthermore, the approach successfully addressed the challenge of integrator accumulation, mitigating potential numerical instability and floating-point errors in digital implementations.

Simulations confirm robust performance of the drive system across various operating conditions, validating the effectiveness of the control design. This performance holds true under steady state, dynamic, and transient conditions, as well as across variable speed, variable torque, and constant power modes.

FIGURE 20. Photograph of the experimental setup.

VII. EXPERIMENTAL IMPLEMENTATION: RESULTS AND DISCUSSION

In the laboratory, an experimental prototype is set up as shown in Fig. 20. A 1 hp four-phase SRM with 8 stator poles and six rotor poles 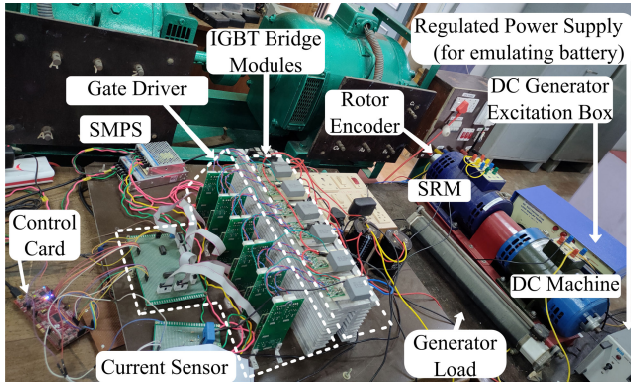is used. A separately excited DC machine is coupled with the SRM for loading. The setup uses six SKM50GB12T4 IGBT modules, with each IGBT module representing one leg of the converter. In each IGBT module, one is used as an IGBT switch, and the body diode of the other IGBT is used as a diode to get the converter, as shown in Fig. 1. Skyper 32R driver is used as the gating circuit for the semiconductor devices. A hollow shaft-type incremental quadrature encoder, ERA50T, connected to the shaft of the machine is used to sense the rotor position. The resolution of the encoder is 1024 pulses per revolution (PPR). One hall current sensor, LA25P, is employed to measure current through the magnetization path (i_{mag}). Signal conditioning for the current sensing circuit is done by MCP6022 op-amp-based differential amplifier circuit. Control implementation for the system is carried out on a DSP microcontroller, the TMS320F28379D.

A. CONTROL ALGORITHM

The digital control algorithm implementation of the proposed scheme involves speed and current control. The clock frequency (f_{clock}) of the TMS320F28379D is 200 MHz [35]. The gating pulses need to be generated according to the commutation sequence. The enhanced quadrature encoder pulse (eQEP) module of the controller is configured in quadrature counter mode. Hence, the counter register (QPOSCNT) counts from 0 to 4096 (4*PPR) in a full mechanical rotation. Speed is calculated by determining the incremental position in a unit time (UT) interval. This time interval for speed measurements should align with the control loop bandwidth (4 Hz), ensuring it is at least twice as fast as the control loop period for timely updates. Additionally, the interval should be less than the time required for traversing a complete rotation at maximum speed. At maximum speed (2000 rpm), the rotor completes one full rotation in 0.03 seconds. Therefore, to calculate speed, the unit timer register of the eQEP

Algorithm 1 Timer ISR for Speed Control System

1: **Position calculation via QEP module:**
   QPOSCNT=Read Position Counter Register.
   Calculate mechanical position and electrical angle:
   $$\theta_m = \frac{360 \, (\text{QPOSCNT})}{4096}$$
   $\theta_e = remainder(\theta_m, 60)$

2: **Speed Calculation:**
   θ_{new} = Read position latch register if the unit timer flag is set.
   $$\omega_{new} = \frac{60(\theta_{new} - \theta_{old})}{4096 \cdot (UT)}; \quad \theta_{old} = \theta_{new}$$

3: **Speed low pass filter:**
   $\omega_{fnew} = k_{\omega f 1}(\omega_{new} + \omega_{old}) + k_{\omega f 2} \cdot \omega_{fold};$
   $\omega_{old} = \omega_{new}; \quad \omega_{fold} = \omega_{fnew}$

4: **Currents Sensing via ADC module:**
   Set SOC and wait for the EOC flag. Acknowledge and reset the EOC flag.
   $i_{new} = \text{ADCRESULT} \cdot k_{ADC}$

5: **Current low pass filter:**
   $i_{fnew} = k_{if1}(i_{new} + i_{old}) + k_{if1} \cdot i_{fold}$
   $i_{old} = i_{new}; \quad i_{fold} = i_{fnew}$

6: **Speed Controller:**
   $\omega_{errnew} = \frac{\pi}{30}(\omega_{ref} - \omega_{fnew})$
   $c_{wnew} = k_{\omega 11}(\omega_{errnew} + \omega_{errold}) + c_{wold};$
   $i_{refnew} = k_{\omega 21} \cdot c_{wnew} - k_{\omega 22} \cdot c_{wold} + k_{\omega 23} \cdot i_{refold}$

7: **Saturation, integral anti-windup and variable updates for speed controller:**
   if ($i_{refnew} > i_{thresh}$) **then**
       $c_{wnew} = c_{wnew} + k_w(i_{thresh} - i_{refnew})$
       $i_{refnew} = i_{thresh}$
   else if ($i_{refnew} < 0$) **then**
       $c_{wnew} = c_{wnew} + k_w \cdot (0 - i_{refnew}); \quad i_{refnew} = 0$
   end if
   $\omega_{errold} = \omega_{errnew}; c_{wold} = c_{wnew}; i_{refold} = i_{refnew};$

8: **Current controller:**
   $i_{errnew} = i_{refnew} - i_{fnew}$
   $c_{inew} = k_{i11}(i_{errnew} + i_{errold}) + c_{iold}$
   $d_{new} = (k_{i21}c_{inew} - k_{i22}c_{iold} + k_{i23}d_{old})$
   $i_{errold} = i_{errnew}; c_{iold} = c_{inew}; d_{old} = d_{new};$

9: **Excitation and commutation sequence:**
   if ($7° < \theta_e < 22°$) **then**
       Phase A
       $\text{CMP}_{T_1} \leftarrow \text{TBPRD}; \text{CMP}_{T_5} \leftarrow d_{new} \cdot \text{TBPRD}$
   else if ($22° < \theta_e < 37°$) **then**
       Phase B
       $\text{CMP}_{T_3} \leftarrow \text{TBPRD}; \text{CMP}_{T_6} \leftarrow d_{new} \cdot \text{TBPRD}$
   else if ($37° < \theta_e < 52°$) **then**
       Phase C
       $\text{CMP}_{T_2} \leftarrow \text{TBPRD}; \text{CMP}_{T_5} \leftarrow d_{new} \cdot \text{TBPRD}$
   else
       Phase D
       $\text{CMP}_{T_4} \leftarrow \text{TBPRD}; \text{CMP}_{T_6} \leftarrow d_{new} \cdot \text{TBPRD}$
   end if

10:   Acknowledge Timer interrupt and return to main program.

Timer ISR

Read ω_{ref}.

$$\theta_m = \frac{360\,(QPOSCNT)}{4096}$$
$$\theta_e = remainder(\theta_m, 60)$$

(UTO=1)? — no → $\omega_{new} = \omega_{old}$

yes

$\theta_{new} = $ [Position Latch register]
$$\omega_{new} = \frac{60(\theta_{new} - \theta_{old})}{4096 \cdot (UT)}$$
$\theta_{old} = \theta_{new}$
Reset UTO Flag.

Speed LPF:
$\omega_{fnew} = k_{\omega f1}(\omega_{new} + \omega_{old}) + k_{\omega f2} \cdot \omega_{fold};$
$\omega_{old} = \omega_{new}; \quad \omega_{fold} = \omega_{fnew}$
Set ADC SOC to read current.

(EOC =1)? — no → Wait

yes

$i_{new} = $ ADCRESULT $\cdot k_{ADC};$
Clear EOC Flag
Current LPF:
$i_{fnew} = k_{if1}(i_{new} + i_{old}) + k_{if1} \cdot i_{fold}$
$i_{old} = i_{new}; \quad i_{fold} = i_{fnew}$

Speed Controller:
$$\omega_{errnew} = \frac{\pi}{30}(\omega_{ref} - \omega_{fnew})$$
$c_{wnew} = k_{\omega 11}(\omega_{errnew} + \omega_{errold}) + c_{wold};$
$i_{refnew} = k_{\omega 21} \cdot c_{wnew} - k_{\omega 22} \cdot c_{wold} + k_{\omega 23} \cdot i_{refold}$

$(i_{refnew} > i_{thresh})$? — yes →
$c_{wnew} = c_{wnew} + k_w(i_{thresh} - i_{refnew})$
$i_{refnew} = i_{thresh}$

no

$(i_{refnew} < 0)$? — yes →
$c_{wnew} = c_{wnew} + k_w \cdot (0 - i_{refnew})$
$i_{refnew} = 0$

no

$\omega_{errold} = \omega_{errnew}; c_{wold} = c_{wnew};$
$i_{refold} = i_{refnew};$

Current controller:
$i_{errnew} = i_{refnew} - i_{fnew}$
$c_{inew} = k_{i11}(i_{errnew} + i_{errold}) + c_{iold}$
$d_{new} = (k_{i21}c_{inew} - k_{i22}c_{iold} + k_{i23}d_{old})$
$i_{errold} = i_{errnew}; c_{iold} = c_{inew}; d_{old} = d_{new};$

$(7° < \theta_e < 22°)$? — yes →
Phase A
$CMP_{T_1} \leftarrow TBPRD$
$CMP_{T_5} \leftarrow d_{new} \cdot TBPRD$

no

$(22° < \theta_e < 37°)$? — yes →
Phase B
$CMP_{T_3} \leftarrow TBPRD$
$CMP_{T_6} \leftarrow d_{new} \cdot TBPRD$

no

$(37° < \theta_e < 52°)$? — yes →
Phase C
$CMP_{T_2} \leftarrow TBPRD$
$CMP_{T_5} \leftarrow d_{new} \cdot TBPRD$

no

Phase D
$CMP_{T_4} \leftarrow TBPRD$
$CMP_{T_6} \leftarrow d_{new} \cdot TBPRD$
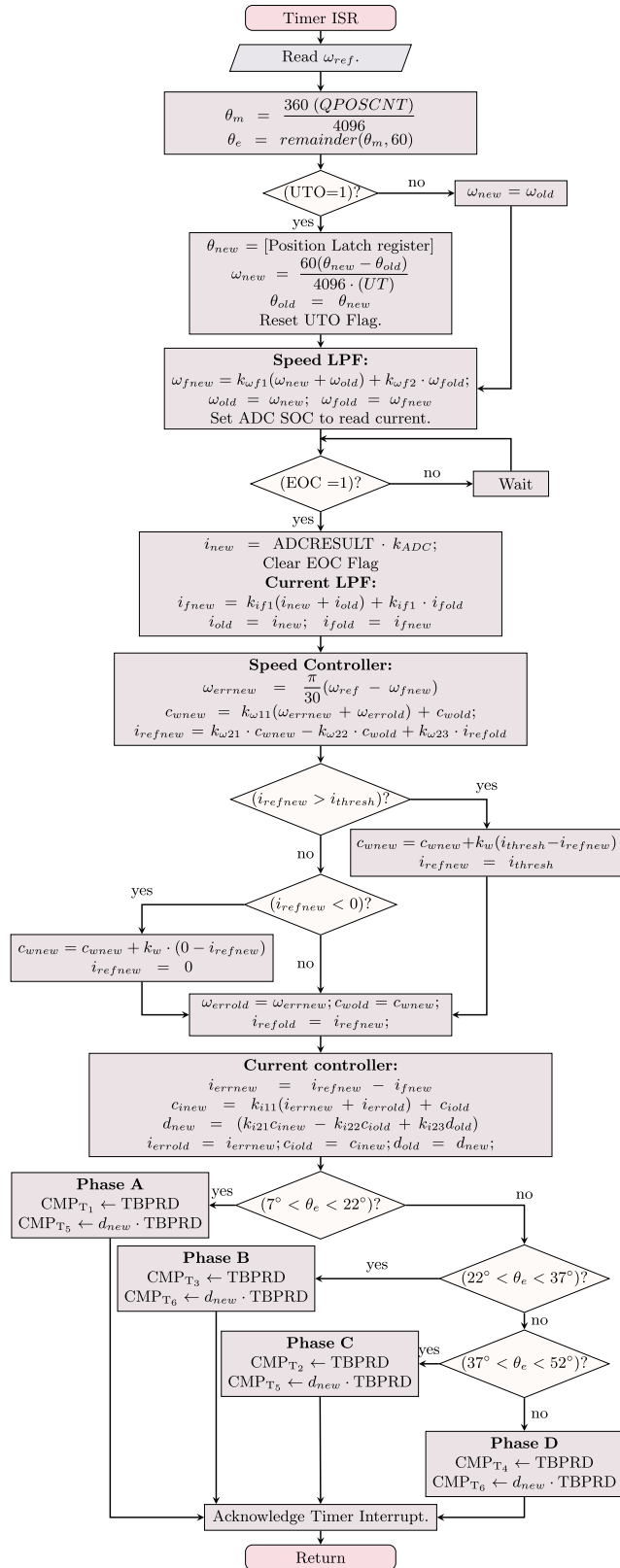
Acknowledge Timer Interrupt.

Return

FIGURE 21. Flowchart of the control implementation within Timer ISR.

module is set to $2 \cdot 10^6 (= 0.01 \cdot f_{clock})$ to achieve a UT of 0.01 seconds. To measure the current, one analog-to-digital

conversion (ADC) pin is configured in a single 12-bit mode. Six ePWM modules are configured in independent mode for a switching frequency of 10 kHz. For this, ePWM prescalers are set to 1, and the ePWM timer base period (TBPRD) register is set with a value of 5000. For synchronizing the control operations, a timer (timer0) is configured for $20\mu s$. Consequently, all the transfer functions, including the speed low pass filter, current low pass filter, speed controller, and current controller, are discretized for a sampling time of $20\ \mu s$. The control algorithm is implemented in the timer interrupt service routine (ISR). Algorithm 1 outlines the timer ISR control algorithm, while Fig. 21 visually showcases its implementation within the timer ISR using a flowchart.

A brief explanation of the algorithm is given below.

1) CALCULATION OF POSITION AND SPEED

First, the position and speed are calculated from the position sensor, as shown in steps 1 and 2 in Algorithm 1. One mechanical rotation of the rotor corresponds to 4096 counts in the QPOSCNT register, measured with respect to the index pulse position from the QEP sensor. In the case of an SRM with six rotor poles, one mechanical rotation translates to six electrical rotations. To determine the excitation and commutation angles, it is essential to predetermine and utilize the appropriate phase. As shown in Fig. 21, the QPOSCNT register's content is latched to the position latch register during each unit timer interrupt (i.e., after every 0.01 s). Consequently, the speed can be calculated by determining rotations per minute from the change in position within the unit time (UT).

2) CURRENT SENSING

The current sensor is connected to the ADC pin. ADC result register is read and multiplied by the calibration factor, k_{ADC} as shown in step 4 of Algorithm 1. The maximum voltage input for the ADC is 3 V, and a 3 V input corresponds to 4095 in the ADC result register. Therefore, by taking into account the sensor gain and the calibration factor mentioned earlier, the ADC result is calibrated to obtain an accurate value.

3) SPEED AND CURRENT LOW PASS FILTERS

The transfer functions in (20) and (21) are discretized using bilinear transformation at a sampling frequency of $20\ \mu s$. The pseudo-code of the digital filters is shown in steps 3 and 5 of Algorithm 1. The constants $k_{\omega f1}$ and $k_{\omega f2}$ pertain to the discretized speed feedback filter, while k_{if1} and k_{if2} correspond to the constants in the discretized current filter.

4) SPEED AND CURRENT CONTROLLERS

The discretized models for the current and speed controllers shown in Fig. 13 and Fig. 14 are implemented in the controller as demonstrated in the steps 6 and 8 in Algorithm 1. As evident in Fig. 14, the integral anti-windup term (k_w) is incorporated to address integral windup issues. In step 7 of Algorithm 1, to implement saturation and integral
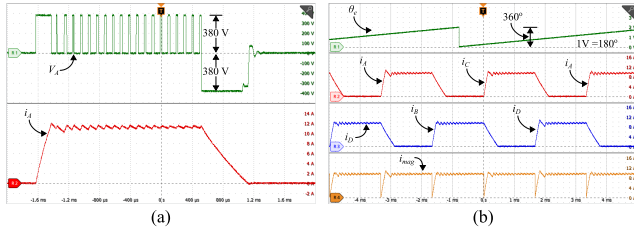
FIGURE 22. Experimental results showing steady state voltage and current waveforms. (a) Phase voltage and phase current at 1200 rpm at rated load. (b) electrical angle, phase currents, and current through magnetization path at 1500 rpm at rated load.

FIGURE 23. Experimental results showing transient speed waveforms and current through the magnetizing path (i_{mag}). (a) Transient waveforms for a step change in speed reference from 0 to 1200 rpm. (b) Transient waveforms for a step change in speed reference from 1400 to 400 rpm.

FIGURE 24. Experimental results showing speed waveforms and current through the magnetizing path (i_{mag}) during dynamic changes. (a) Dynamic waveforms for step changes in reference speed (1500 rpm, 500 rpm, and 1000 rpm). (b) Waveforms for dynamic changes in the load torque.

anti-windup, it is first checked if the value of i_{refnew} exceeds a predefined threshold band (i_{thresh} and zero). If it does, c_{wnew} saturates due to the windup term, and i_{refnew} is set to the threshold value.

5) PHASE CURRENT CONTROL

As in step 9 of Algorithm 1, the output of the current controller (d_{new}) represents the duty cycle to be applied to either switches T_1 or T_2, depending on the phase that needs to be excited. The determination of the phase to be excited is made in advance based on predetermined excitation and commutation angles. Consequently, the product of the duty cycle and TBPRD is directed to the compare (CMP) register of the corresponding ePWM. Simultaneously, as one of the bottom switches (T_1, T_2, T_3, T_4) are active throughout their respective phase conduction period, TBPRD is fed into their corresponding compare registers.

B. RESULTS AND DISCUSSION

The performance of the proposed SRM drive is assessed using the experimental prototype, examining both steady-state and dynamic behavior. In Fig. 22, steady-state experimental waveforms are presented. Fig. 22(a) illustrates voltage and current waveforms at 1200 rpm, with a switching frequency of 10 kHz. The results align with the simulation results presented. The current controller successfully regulates phase current within acceptable limits without employing hysteresis control, showcasing its effectiveness as a simpler and more reliable alternative to hysteresis or delta modulation techniques. Fig. 22(b) demonstrates the successful decoupling of the demagnetizing current, showcasing the efficacy of control using a single sensor. To visualize this, the digital-to-analog (DAC) channel within the DSP microcontroller is configured to display electrical rotor angle waveforms on the digital storage oscilloscope (DSO). Current probes are positioned along the two common connections for alternate phases. The waveform of the current through the magnetizing path i_{mag}), which is sensed for closed-loop operation, is also measured using a current probe. The results affirm the successful decoupling of the demagnetizing current. It is evident from the waveforms that the current through the individual phases can be controlled by controlling the current through the magnetizing path, when there is no overlap between phases in the conduction period.
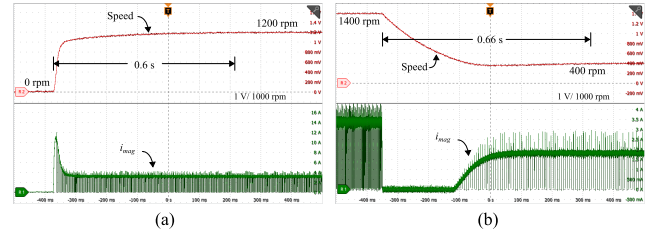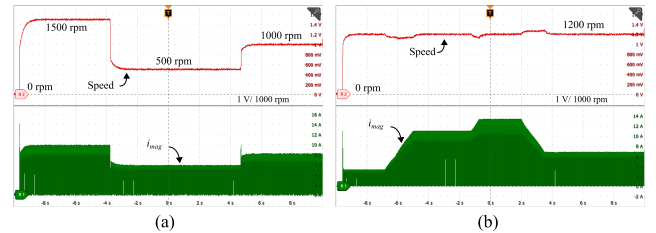
To examine the transient behavior of the proposed drive, its performance is analyzed with a step change in the speed reference. The speed is displayed on the DSO by configuring the Digital-to-Analog Converter (DAC) channel within the DSP microcontroller. In Fig. 23, transient speed waveforms and current through the magnetizing path (i_{mag}) for step changes in speed reference are presented. Fig. 23(a) illustrates transient waveforms for a step change in speed reference from 0 to 1200 rpm under no load conditions. The motor starts from rest and achieves the reference speed of 1200 rpm, stabilizing within 0.6 seconds with no overshoot. Fig. 23(b) shows waveforms for a step change in speed reference from 1400 to 400 rpm under no load conditions, with the trajectory stabilizing at 400 rpm within 0.66 seconds, exhibiting a minor undershoot.

The dynamic behavior of the drive is further explored with variations in reference speed and load torque. Load torque is varied by adjusting the excitation to the DC machine coupled with the SRM, with the rheostat connected to the DC machine armature set to its maximum position. In Fig. 24, waveforms of speed and current through the magnetizing path (i_{mag}) during dynamic changes in speed and load torque are presented. Fig. 24(a) displays dynamic waveforms for step changes in reference speed (1500 rpm, 500 rpm, and 1000 rpm) starting from rest, with constant excitation and load resistance. Smooth speed trajectories are observed with no overshoots or undershoots. Fig. 24(b) illustrates the speed and i_{mag} during constant speed operation (1200 rpm) with dynamic load changes. Variations in load result in minor speed fluctuations, and the system tracks back to the reference speed without delay, indicating minimal overshoots or undershoots. These dynamic operation results align with

simulation results, emphasizing the proposed drive's ability to operate under diverse conditions.

Experimental results align with simulation findings, further solidifying the observed robust performance of the drive system across various operating conditions, including steady state, dynamic, and transient scenarios. This confirms the effectiveness of the control design, demonstrating its consistent robustness under dynamic step speed and load torque variations.

VIII. CONCLUSION

This paper presents a systematic approach to digital control development for a four-phase SRM drive for medium power applications. Medium-power applications demand efficient and cost-effective control solutions for SRM drives. However, existing literature often lacks a detailed and comprehensive control development procedure, considering the need to minimize cost and complexity. Addressing this gap, this paper introduces a novel SRM drive combining a Miller converter-fed motor with a single current sensor, specifically designed for medium-power applications. A systematic control development procedure is presented for the drive, covering mathematical modeling of the motor and converter, design procedures, dynamic simulation, analysis, and experimental validation.

An accurate MATLAB Simulink simulation model of the SRM is obtained by FEA using Ansys. Subsequent parametric simulation studies is utilized for optimizing conduction angle. For control design, a reliable linear model of the SRM is obtained using small signal analysis. Speed and current controllers are then designed using the K-factor method. Additionally, the paper presents the detailed control algorithm developed, targeting the TMS320F28379D DSP microcontroller, for the proposed SRM drive.

Simulations and experiments effectively validate the proposed drive's performance across diverse operating conditions, including steady-state operation, dynamic speed changes, and transient load variations. Simulations confirmed the drive's effectiveness in both constant torque (below base speed) and constant power (above base speed) operating regions. Due to the DC machine's speed limit, experiments focused on variable speed and load variations below base speed. These experiments demonstrated a settling time of around 1.6 seconds for a speed step change from 0 to 1200 rpm and around 1.66 seconds for a step change from 1400 to 400 rpm. Moreover, the experimental results showcase the drive's robust speed tracking even during dynamic speed changes and load variations, aligning with the simulation findings and validating its effectiveness.

Looking forward, further research could focus on position sensorless control strategies and torque ripple minimization strategies for medium-power applications. Although these strategies are discussed in the literature, further investigation into developing cost-effective strategies with reduced current sensors and computational intensity remains relevant. Additionally, for battery-powered medium-power EVs, SRM based integrated onboard chargers reutilizing the motor windings, SRM converter and the current sensor presents a promising avenue for further reduction in overall cost in SRM applications for medium power EVs.

REFERENCES

[1] Z. Q. Zhu and D. Howe, "Electrical machines and drives for electric, hybrid, and fuel cell vehicles," *Proc. IEEE*, vol. 95, no. 4, pp. 746–765, Apr. 2007.

[2] K. M. Rahman, B. Fahimi, G. Suresh, A. V. Rajarathnam, and M. Ehsani, "Advantages of switched reluctance motor applications to EV and HEV: Design and control issues," *IEEE Trans. Ind. Appl.*, vol. 36, no. 1, pp. 111–121, 2000.

[3] K. T. Chau, C. C. Chan, and C. Liu, "Overview of permanent-magnet brushless drives for electric and hybrid electric vehicles," *IEEE Trans. Ind. Electron.*, vol. 55, no. 6, pp. 2246–2257, Jun. 2008.

[4] B. Bilgin, J. W. Jiang, and A. Emadi, *Switched Reluctance Motor Drives: Fundamentals to Applications*. Boca Raton, FL, USA: CRC Press, 2019.

[5] I. Boldea, L. N. Tutelea, L. Parsa, and D. Dorrell, "Automotive electric propulsion systems with reduced or no permanent magnets: An overview," *IEEE Trans. Ind. Electron.*, vol. 61, no. 10, pp. 5696–5711, Oct. 2014.

[6] B. Bilgin, B. Howey, A. D. Callegaro, J. Liang, M. Kordic, J. Taylor, and A. Emadi, "Making the case for switched reluctance motors for propulsion applications," *IEEE Trans. Veh. Technol.*, vol. 69, no. 7, pp. 7172–7186, Jul. 2020.

[7] B. Singh, A. K. Mishra, and R. Kumar, "Solar powered water pumping system employing switched reluctance motor drive," *IEEE Trans. Ind. Appl.*, vol. 52, no. 5, pp. 3949–3957, Sep. 2016.

[8] A. K. Mishra and B. Singh, "High gain single ended primary inductor converter with ripple free input current for solar powered water pumping system utilizing cost-effective maximum power point tracking technique," *IEEE Trans. Ind. Appl.*, vol. 55, no. 6, pp. 6332–6343, Nov. 2019.

[9] R. Krishnan, *Switched Reluctance Motor Drives: Modeling, Simulation, Analysis, Design, and Applications*. Boca Raton, FL, USA: CRC Press, 2017.

[10] V. F. Pires, A. J. Pires, A. Cordeiro, and D. Foito, "A review of the power converter interfaces for switched reluctance machines," *Energies*, vol. 13, no. 13, p. 3490, Jul. 2020.

[11] F. Peng, J. Ye, and A. Emadi, "An asymmetric three-level neutral point diode clamped converter for switched reluctance motor drives," *IEEE Trans. Power Electron.*, vol. 32, no. 11, pp. 8618–8631, Nov. 2017.

[12] C. Pollock and B. W. Williams, "Power convertor circuits for switched reluctance motors with the minimum number of switches," *IEE Proc. B Electric Power Appl.*, vol. 137, no. 6, p. 373, 1990.

[13] D. Xiao, S. R. Filho, G. Fang, J. Ye, and A. Emadi, "Position-sensorless control of switched reluctance motor drives: A review," *IEEE Trans. Transport. Electrific.*, vol. 8, no. 1, pp. 1209–1227, Mar. 2022.

[14] J. Ye, B. Bilgin, and A. Emadi, "Elimination of mutual flux effect on rotor position estimation of switched reluctance motor drives considering magnetic saturation," *IEEE Trans. Power Electron.*, vol. 30, no. 2, pp. 532–536, Feb. 2015.

[15] G. Pasquesoone, R. Mikail, and I. Husain, "Position estimation at starting and lower speed in three-phase switched reluctance machines using pulse injection and two thresholds," *IEEE Trans. Ind. Appl.*, vol. 47, no. 4, pp. 1724–1731, Jul. 2011.

[16] F. Peng, J. Ye, A. Emadi, and Y. Huang, "Position sensorless control of switched reluctance motor drives based on numerical method," *IEEE Trans. Ind. Appl.*, vol. 53, no. 3, pp. 2159–2168, May 2017.

[17] C. Gan, Q. Sun, N. Jin, L. M. Tolbert, Z. Ling, Y. Hu, and J. Wu, "Cost-effective current measurement technique for four-phase SRM control by split dual bus line without pulse injection and voltage penalty," *IEEE Trans. Ind. Electron.*, vol. 65, no. 6, pp. 4553–4564, Jun. 2018.

[18] C. Gan, J. Wu, Y. Hu, S. Yang, W. Cao, and J. L. Kirtley, "Online sensorless position estimation for switched reluctance motors using one current sensor," *IEEE Trans. Power Electron.*, vol. 31, no. 10, pp. 7248–7263, Oct. 2016.

[19] P. Kumar, M. Israyelu, and S. Sashidhar, "A simple four-phase switched reluctance motor drive for ceiling fan applications," *IEEE Access*, vol. 11, pp. 7021–7030, 2023.

[20] S. Xu, H. Chen, J. Yang, and F. Dong, "Comparative evaluation on switched reluctance motor drive with different phase current sensing methods," *IET Electr. Power Appl.*, vol. 13, no. 12, pp. 1964–1975, Dec. 2019.

[21] B. K. Bose, T. J. E. Miller, P. M. Szczesny, and W. H. Bicknell, "Microcomputer control of switched reluctance motor," *IEEE Trans. Ind. Appl.*, vol. IA-22, no. 4, pp. 708–715, Jul. 1986.

[22] R. Samudio and P. Pillay, "Design of a flexible DSP-based drive development system," in *Proc. IAS Conf. Rec. IEEE Ind. Appl. Conf. 13th IAS Annu. Meeting*, Oct. 1995, pp. 1854–1861.

[23] H. K. Bae and R. Krishnan, "A study of current controllers and development of a novel current controller for high performance SRM drives," in *Proc. IAS Conf. Rec. IEEE Ind. Appl. Conf. 31st IAS Annu. Meeting*, Oct. 1996, pp. 68–75.

[24] M. Ilic'-Spong, R. Marino, S. Peresada, and D. Taylor, "Feedback linearizing control of switched reluctance motors," *IEEE Trans. Autom. Control*, vol. AC-32, no. 5, pp. 371–379, May 1987.

[25] R. B. Inderka and R. W. A. A. De Doncker, "DITC-direct instantaneous torque control of switched reluctance drives," *IEEE Trans. Ind. Appl.*, vol. 39, no. 4, pp. 1046–1051, Jul. 2003.

[26] M. V. de Paula and T. A. d. S. Barros, "A sliding mode DITC cruise control for SRM with steepest descent minimum torque ripple point tracking," *IEEE Trans. Ind. Electron.*, vol. 69, no. 1, pp. 151–159, Jan. 2022.

[27] F. Peng, J. Ye, and A. Emadi, "A digital PWM current controller for switched reluctance motor drives," *IEEE Trans. Power Electron.*, vol. 31, no. 10, pp. 7087–7098, Oct. 2016.

[28] S. Dhale, B. Nahid-Mobarakeh, and A. Emadi, "A review of fixed switching frequency current control techniques for switched reluctance machines," *IEEE Access*, vol. 9, pp. 39375–39391, 2021.

[29] S. S. Ahmad and G. Narayanan, "Linearized modeling of switched reluctance motor for closed-loop current control," *IEEE Trans. Ind. Appl.*, vol. 52, no. 4, pp. 3146–3158, Jul. 2016.

[30] K. A. Khan and M. Khalid, "Improving the transient response of hybrid energy storage system for voltage stability in DC micro-grids using an autonomous control strategy," *IEEE Access*, vol. 9, pp. 10460–10472, 2021.

[31] H. Le-Huy and P. Brunelle, "A versatile nonlinear switched reluctance motor model in simulink using realistic and analytical magnetization characteristics," in *Proc. 31st Annu. Conf. IEEE Ind. Electron. Soc. (IECON)*, Nov. 2005, p. 6.

[32] H. Hannoun, M. Hilairet, and C. Marchand, "Analytical modeling of switched reluctance machines including saturation," in *Proc. IEEE Int. Electric Mach. Drives Conf.*, May 2007, pp. 564–568.

[33] S. Tarbouriech and M. Turner, "Anti-windup design: An overview of some recent advances and open problems," *IET Control Theory Appl.*, vol. 3, no. 1, pp. 1–19, Jan. 2009.

[34] A. Visioli, *Practical PID Control*. Cham, Switzerland: Springer, 2006.

[35] *Technical Reference Manual: TMS320F2837xD Dual-Core Microcontrollers*, Texas Instruments, Dallas, TX, USA, 2019. [Online]. Available: https://www.ti.com/lit/pdf/spruhm8

D. ARUN DOMINIC (Member, IEEE) received the B.E. and M.E. degrees in electrical and electronics engineering from Anna University, Chennai, in 2006 and 2008, respectively, and the Ph.D. degree from the Indian Institute of Technology, Roorkee, in 2016, with a focus on fault tolerance control of electrical drives.

From 2008 to 2011, he was an Assistant Professor with the Loyola Institute of Technology and Science Thovalai, Kanyakumari, and Noorul Islam University, Kumaracoil, Kanyakumari. Then, he was an Ad-Hoc Faculty Member with the National Institute of Technology Jalandhar, from 2016 to 2018, and the National Institute of Technology Warangal, from 2018 to 2019. Since 2019, he has been an Assistant Professor with the Department of Electrical and Electronics Engineering, National Institute of Technology Karnataka, Surathkal. His research interests include electrical drives, power electronics, electric vehicles, and fault tolerance control of electrical drives.

T. FAHEEM ALI (Graduate Student Member, IEEE) received the B.Tech. degree in electrical and electronics engineering from the Rajiv Gandhi Institute of Technology, Kottayam, in 2013, and the M.Tech. degree in power electronics and drives from the Government College of Engineering, Kannur, in 2016. He is currently pursuing the Ph.D. degree with the National Institute of Technology Karnataka, Surathkal.

He was an Assistant Professor with the MEA Engineering College, Malappuram, from 2016 to 2019. His research interests include power electronics, electric drives, and on-board chargers.

PRAJOF PRABHAKARAN (Senior Member, IEEE) received the B.Tech. degree in electrical and electronics engineering and the M.Tech. degree in power electronics from Amrita Vishwa Vidyapeetham (Amrita University), Coimbatore, in 2009 and 2011, respectively, and the Ph.D. degree in electrical engineering from the Indian Institute of Technology Bombay, Mumbai, in 2018, with a focus on DC microgrids.

From 2011 to 2013, he was an Assistant Professor with the Electrical and Electronics Engineering Department, Amrita School of Engineering, Coimbatore. After a brief stint with the National Institute of Technology Calicut, Kozhikode, as an Ad-Hoc Faculty Member, in 2018, he joined the Transportation Solutions Department, L&T Technological Services, Bengaluru, where he worked for a year as a Project Lead for the research and development of powertrain and battery management system for electric vehicle. Since 2019, he has been an Assistant Professor with the Department of Electrical and Electronics Engineering, National Institute of Technology Karnataka, Surathkal. His research interests include power electronics, renewable energy, electric vehicles, and microgrids.

· · ·